Thermal Characterization of Ferroelectric Al$_{1-x}$B$_x$N for Nonvolatile Memory

Kyuhwe Kang, Joseph A. Casamento, Daniel C. Shoemaker, Yiwen Song, Erdem Z. Ozdemir, Nathaniel S. McIlwaine, Jon-Paul Maria, Sukwon Choi,* and Susan E. Trolier-McKinstry*

Cite This: *ACS Appl. Mater. Interfaces* 2024, 16, 67921−67933

Read Online

ACCESS | Metrics & More | Article Recommendations

ABSTRACT: Boron (B)-substituted wurtzite AlN (Al$_{1-x}$B$_x$N) is a recently discovered wurtzite ferroelectric material that offers several advantages over ferroelectric Hf$_{1-x}$Zr$_x$O$_2$ and PbZr$_{1-x}$Ti$_x$O$_3$. Such benefits include a relatively low growth temperature as well as a thermally stable, and thickness-stable ferroelectric polarization; these factors are promising for the development of ferroelectric nonvolatile random-access memory (FeRAM) that are CMOS-compatible, scalable, and reliable for storing data in harsh environments. However, wurtzite ferroelectric materials may undergo exacerbated self-heating upon polarization switching relative to other ferroelectric materials; the larger energy loss is anticipated due to the higher coercive field and remanent polarization. This work provides insight into the polarization switching-induced self-heating of future FeRAM based on Al$_{1-x}$B$_x$N. It was experimentally observed that the thermal conductivity of Al$_{1-x}$B$_x$N thin films drops from 40.9 W m^{-1} K^{-1} to 4.35 W m^{-1} K^{-1} (which is 2 orders of magnitude lower than that of bulk AlN) when the B composition (x) increases from 0 to 0.18. The transient thermal response of an Al$_{0.93}$B$_{0.07}$N metal−ferroelectric−metal (MFM) capacitor was investigated using micro-Raman thermometry and validated via device thermal modeling. Further simulation studies reveal that the large heat generation rate and the low thermal conductivity is predicted to induce an instantaneous temperature rise that may exceed 150 °C in a FeRAM device based on a 5 nm thick Al$_{1-x}$B$_x$N film at GHz frequency switching. In addition, thermal crosstalk within a FeRAM cell array exacerbates the self-heating, resulting in a predicted steady-state temperature rise that is an order of magnitude higher than that of a single bit-cell.

KEYWORDS: aluminum boron nitride, device self-heating, ferroelectric random-access memory, polarization switching, thermal conductivity, time-domain thermoreflectance, transient Raman thermometry
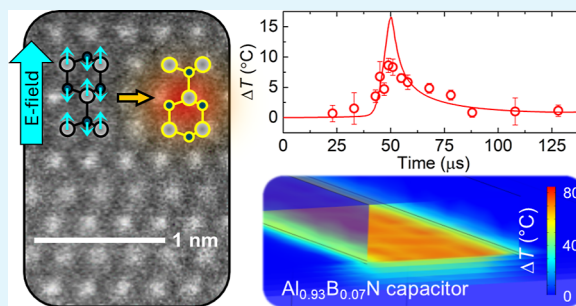
1. INTRODUCTION

Aluminum nitride (AlN), a wurtzite III−V compound, has been utilized in various technology fields because of its wide bandgap, strong piezoelectric response, high temperature tolerance, low dielectric loss, and well-established growth and etching processes. Alloying has often been used to enhance the functionality of AlN. For instance, Al$_x$Ga$_{1-x}$N is the base material for ultraviolet optoelectronics[1] and wide/ultrawide electronic devices.[2] Similarly, Al$_{1-x}$Sc$_x$N has enabled wide bandwidth acoustic resonators.[3,4]

Recently, it has been observed that AlN and some of its solid solutions exhibit ferroelectric properties[5−7] with large coercive fields (>2 MV cm^{-1}) and remanent polarizations (>80 μC cm^{-2}). These values are larger than those for most perovskite- and HfO$_2$-based ferroelectric materials.[5,8,9] Ferroelectric AlN-based solid solutions offer several benefits compared to other ferroelectric materials. First, the low growth temperatures (<400 °C) enable the complementary metal oxide semiconductor (CMOS) back-end-of-line (BEOL) compatibility.[10,11] Second, the thermal stability of the ferroelectric

polarization is better than those for other ferroelectric materials[12] including fluorite and perovskite compounds, that are susceptible to loss of written polarization states when the materials are heated.[13] The wurtzite crystal structure is stable up to the melting temperature (2200−3000 °C)[14] and there are no known temperature-driven transitions to a nonpolar polytype structure.[15,16] Third, the strong propensity for texturing during film growth (Figure 1a) results in a minimal reduction in the polarization for nm-range thick films that are necessary to construct highly scaled devices.[17]
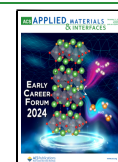
Wurtzite ferroelectrics are candidates for ferroelectric nonvolatile random-access memory (FeRAM) applications,[18−20] where the direction of ferroelectric polarization is
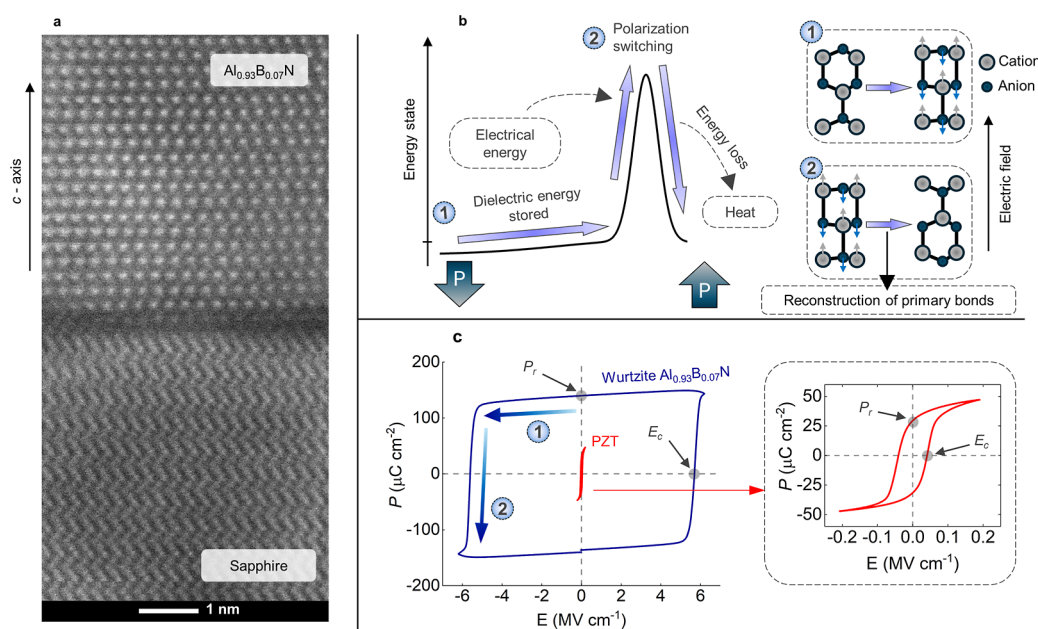
Figure 1. Energy loss and self-heating in ferroelectric wurtzite $Al_{0.93}B_{0.07}N$. (a) Cross-sectional scanning transmission electron microscopy (STEM) image of $Al_{0.93}B_{0.07}N$ grown on a sapphire. (b) The self-heating mechanism in ferroelectric wurtzite materials via polarization switching. ① When an electric field is applied, dielectric energy is stored by the materials system. ② When the applied electric field reaches the coercive field, a significant amount of electrical energy is absorbed by the material to break and rebuild the primary bonds during the switching process. The absorbed energy is irreversibly converted to the waste heat during this deformation process. The insets on the right show the deformation of the crystal structure during steps ① and ②. (c) Polarization-electric field hysteresis loops of wurtzite $Al_{0.93}B_{0.07}N$ (blue loop) and $Pb_{0.99}(Zr_{0.52}Ti_{0.48})_{0.98}Nb_{0.02}O_3$ (PZT-red loop) noted with the remanent polarization (P_r) and the coercive field (E_c) values. The circled numbers correspond to the physical mechanisms illustrated in (b).

used as a means of binary data storage. FeRAM devices based on lead zirconate titanate (PZT) and strontium bismuth tantalate (SBT) have been commercially available for more than a decade, although their use is currently limited due to the low data density. The scalability of ferroelectric wurtzite materials gives promise to the realization of high data density FeRAM.

Wurtzite-based FeRAM also offers potential advantages for harsh environment operation, especially for space applications. Charge-based data storage technologies are vulnerable to high-energy cosmic particle irradiation (γ-ray, electrons, protons, etc.) in space.[21] It requires a radiation-hardened microprocessor design which demotes its performance. For instance, RAD750 (which is a radiation-hardened computer system developed 23 years ago) continues to be deployed for new launches. Although several technologies that are robust to irradiation were developed for space applications, their data retention time strongly depends on the ambient temperature. In a spacecraft, temperature regulation can be challenging. Since wurtzite-based FeRAM offers the potential for robustness to irradiation and thermal stability, it is of interest for reliable data storage in space.

Despite all the benefits offered by wurtzite-based FeRAM, there is a noticeable disadvantage. The amount of energy loss that occurs upon polarization switching is expected to be significantly larger than that of PZT or SBT. Polarization switching, or any field excursion that produces irreversible domain nucleation and domain wall motion, in ferroelectric materials is accompanied by energy dissipation.[22−24] Figure 1b illustrates the energy loss mechanism during polarization switching in wurtzite ferroelectric materials using an energy state diagram. Upon the application of an electric field,

dielectric energy arising from the ionic and electronic polarizabilities is stored in the material system without a ferroelectric response. This energy reversibly converts back to electrical energy when the electric field is removed (AlN has an intrinsic dissipation factor smaller than $0.0005^{[25−28]}$). In contrast, when the electric field magnitude reaches the material's coercive field (E_c), polarization switching occurs due to the dipolar polarizability. This mechanism requires a large amount of energy since it is accompanied by reconstruction of some of the primary bonds.[29] Once the polarization is switched, the energy state returns to a stable state by releasing the stored energy as heat. Figure 1c illustrates the energy storage and release mechanisms that occur within a polarization-electric field hysteresis loop ($P−E$ hysteresis loop). The amount of volumetric heat generation (energy loss) from polarization switching can be calculated based on the area inside the $P−E$ hysteresis loop.[30] The larger the area, the more energy is lost per cycle. Because the area is approximately proportional to E_c and the remanent polarization (P_r), the volumetric heat generation (per cycle) in wurtzite ferroelectric materials can be two to 3 orders of magnitude larger than those for conventional ferroelectric materials such as PZT, as shown in the inset of Figure 1c.

Any rise in FeRAM temperature has undesired consequences in terms of device performance and reliability. For example, in PZT capacitors, high ambient temperature conditions (105−250 °C) result in a decrease in the polarization, coercive field, and the polarization (data) retention lifetime, while also leading to an "imprint" in the $P−E$ hysteresis loop that shifts E_c and P_r.[31] In addition, an increase in the ambient temperature is accompanied by an increase in leakage currents[31] that can obscure the polarization switching current essential for reading
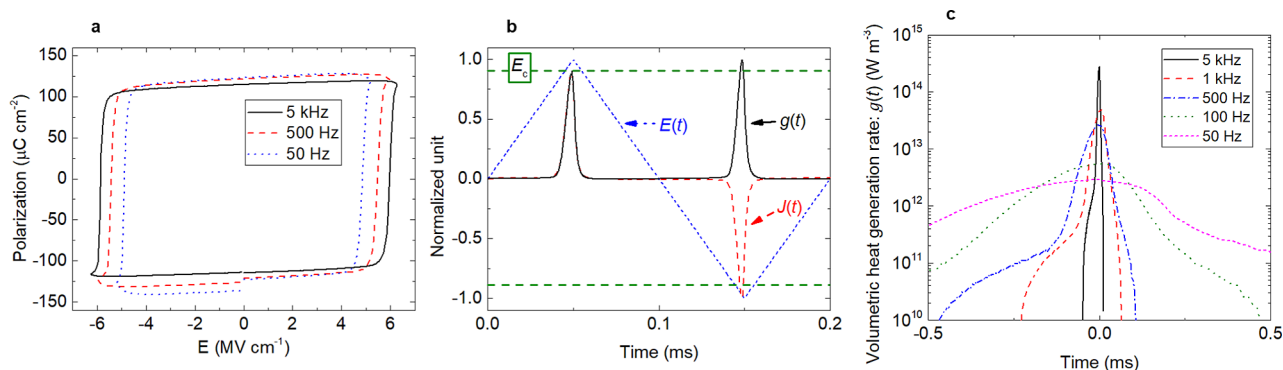
Figure 2. Ferroelectric characteristics of a 300 nm thick $Al_{0.93}B_{0.07}N$ film. (a) Polarization-electric field hysteresis loops. (b) Measurement of the applied electric field $E(t)$, current density $J(t)$, and the power loss density (volumetric heat generation rate) $g(t)$ for 5 kHz operation. E_c is 5.91 MV cm^{-1}. (c) Measured time-dependent volumetric heat generation rates for four different operational frequencies.

FeRAMs. The relatively low memory density and coercive fields of PZT and SBT render self-heating (caused by polarization switching) to be a modest problem for current FeRAM devices. However, the self-heating effect in wurtzite-based FeRAM devices should be thoroughly investigated, due to their comparatively large energy loss per cycle, to ensure reliable device operation and to perform design optimization.

To study polarization switching-induced self-heating, thermal characterization of $Al_{1-x}B_xN$ thin films grown by a magnetron cosputtering and metal−ferroelectric−metal (MFM) capacitors fabricated based on these films was performed. Currently, two group III-nitride solid solutions that are candidates for FeRAM applications have been reported: $Al_{1-x}Sc_xN$ and $Al_{1-x}B_xN$. $Al_{1-x}Sc_xN$ allows modification of E_c and P_r by adjusting the alloy composition (x); however, Sc is a comparatively expensive material, and $Al_{1-x}Sc_xN$ films are also prone to contamination by oxygen. $Al_{1-x}B_xN$ utilizes less expensive and fully CMOS-compatible constituents and offers a larger bandgap energy than $Al_{1-x}Sc_xN$.[32] However, this materials system has not been studied as extensively.[33]

The self-heating of an $Al_{1-x}B_xN$ device depends on the thermal conductivity (κ), which dictates the effectiveness of transporting the heat away from the device active region. While the κ of $Al_{1-x}Sc_xN$ has been reported,[34] experimental data for $Al_{1-x}B_xN$ is lacking. In the first part of this work, the cross-plane thermal conductivity ($\kappa_\perp$; along the c-axis) of $Al_{1-x}B_xN$ thin films was measured as a function of B-composition (x), thickness, and temperature. The measurement results were confirmed using a thermal conductivity model based on Callaway's phonon gas theory,[35−37] augmented by a virtual crystal approximation (VCA).

VCA includes a resistive phonon scattering process arising from the chemical disorder associated with the cation sublattice, i.e., phonon-alloy disorder scattering.[38] In the second part of this work, the self-heating effect in an $Al_{1-x}B_xN$ MFM capacitor induced by polarization switching was characterized using micro-Raman thermometry. Experimental results were validated using a device thermal model. Finally, simulation of a hypothetical high-density $Al_{1-x}B_xN$ FeRAM array was performed to study its transient thermal response. This model was used to interrogate factors that impact the self-heating behavior such as the $Al_{1-x}B_xN$ film thickness, clock speed for data writing, and the thermal crosstalk between adjacent bit-cells.

2. HEAT GENERATION INDUCED BY POLARIZATION SWITCHING

As explained above, heat generation via the nucleation of new domains and the motion of domain walls is a characteristic phenomenon for ferroelectric materials. The volumetric energy loss for a round-trip of polarization switching corresponds to the internal area of a $P−E$ hysteresis loop. This area depends on the field sweep frequency (Figure 2a), temperature,[6] defect concentrations, etc. The time-averaged volumetric heat generation rate (g_{avg}) driven by an alternating current (AC) electric field can be expressed as shown in eq 1.

$$g_{avg} = f \oint g(t)\, \mathrm{d}t = f \oint E(t) \cdot J(t)\, \mathrm{d}t = f \oint E(P)\, \mathrm{d}P \qquad (1)$$

where $g(t)$ is the volumetric heat generation rate as a function of time, f is the frequency of the AC electric field, and $J(t)$ is the current density. When only polarization switching contributes to the current density, eq 2 is valid. Equation 3 is obtained by substituting $J(t)$ into eq 1.

$$J(t) = \frac{\mathrm{d}P}{\mathrm{d}t} \qquad (2)$$

$$g_{avg} = f \oint E(P)\, \mathrm{d}P \qquad (3)$$

g_{avg} can be used to evaluate the steady-state temperature rise of a ferroelectric film driven by an AC electric field. However, it should be noted that in practice, the volumetric heat generation rate is a function of time, $g(t)$. In Figure 2b, $g(t)$ is manifested by a short pulse of heat generation, a product of the measured $E(t)$ and $J(t)$ with respect to time. The $g(t)$ pulse occurs when the applied electric field approaches E_c (5−6 MV cm^{-1} for $Al_{1-x}B_xN$)[33] and polarization is switched. The expression $g(t) = E(t) \times J(t)$ assumes that the energy loss is instantaneously manifested by heat generation.

Figure 2c depicts the measured $g(t)$ of a 300 nm thick $Al_{0.93}B_{0.07}N$ layer driven by bipolar triangular electric fields with four different frequencies and peak amplitudes of 6−6.6 MV cm^{-1}. It is observed that $g(t)$ is more concentrated for higher frequency operation, so that $g(t)$ has a larger peak intensity and a narrower width. When the electric field ramp rate is higher (i.e., shorter rise time), the required E_c is higher and the polarization switching speed is faster; thus the width of $J(t)$ is narrower (eq 2). The larger peak intensity of a heat generation pulse for higher frequency operation is expected to
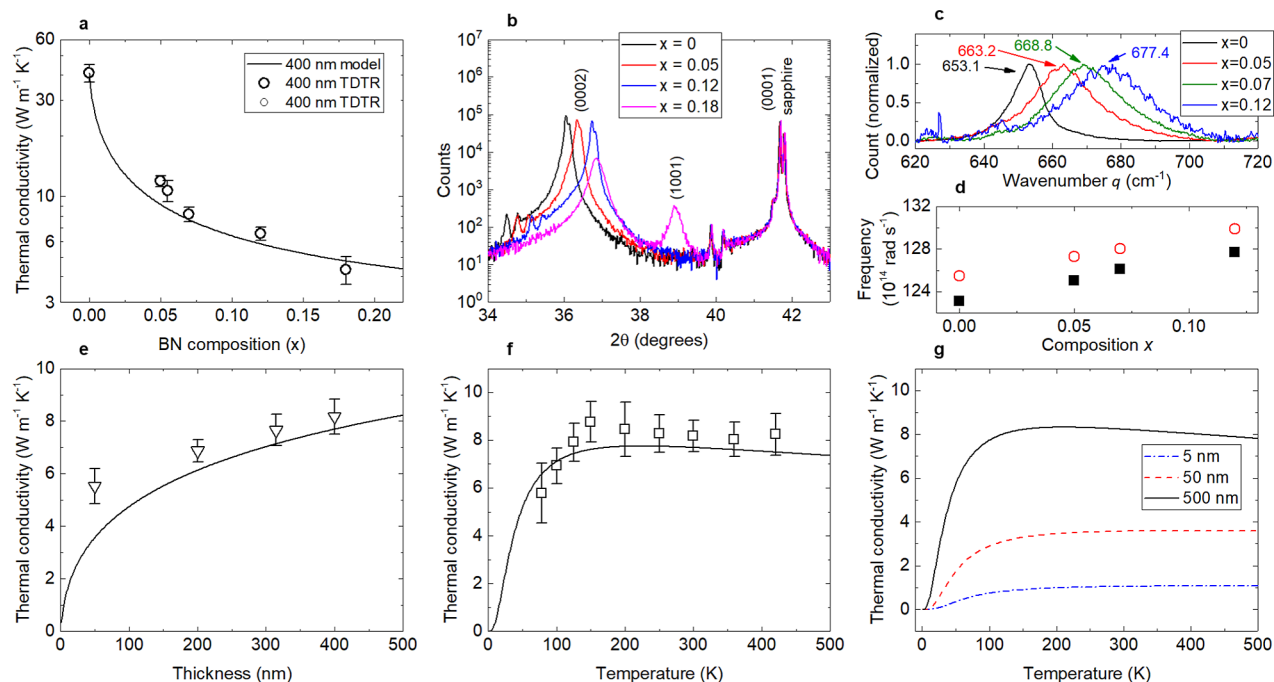
Figure 3. Characterization of $Al_{1-x}B_xN$ layers. (a−d) Measurements and calculations of 400 nm thick $Al_{1-x}B_xN$ layers with different B-compositions, x: (a) cross-plane thermal conductivities, where the symbols and line represent results from TDTR measurements and phonon gas modeling, respectively, (b) XRD theta-2theta scan for a range where (0002) and (1001) peaks of $Al_{1-x}B_xN$ can be observed, (c) the measured E_2 (high) phonon peaks of four $Al_{1-x}B_xN$ films using Raman spectroscopy, and (d) the E_2 (high) phonon frequencies measured via Raman spectroscopy (filled squares) and calculated using the thermal conductivity model (open circles). (e−g) Measurement (symbols) and calculation (line) results of the cross-plane thermal conductivity of $Al_{0.93}B_{0.07}N$ as a function of film thickness at room temperature (e) and a function of temperature, where film thickness is 400 nm (f) or 5−500 nm (g).

result in a significantly increased instantaneous peak temperature of the ferroelectric film.

It should be noted that the leakage current flowing through the ferroelectric layer can hinder the quantification of heating caused by polarization switching. According to eq 2, a relatively large leakage current vertically expands the hysteresis loop, where the loop area (i.e., the volumetric energy loss) includes a notable contribution from Joule heating. Therefore, the hysteresis loop and polarization switching current data shown in Figure 2 were collected with the following criterion. The amplitude of the AC field was applied to be "0.4 MV cm^{-1} + E_c" to suppress the leakage current.

3. THERMAL CODNCUTIVITY OF $AL_{1-x}B_xN$

The cross-plane thermal conductivity ($\kappa_\perp$) of 400 nm thick $Al_{1-x}B_xN$ samples with different x was characterized using a time-domain thermoreflectance (TDTR) method. It was reported that ferroelectricity is observed for B-compositions of $0 \leq x \leq 0.19$.[33] Therefore, six $Al_{1-x}B_xN$ films with an x of 0, 0.05, 0.06, 0.07, 0.12, and 0.18 were prepared via reactive magnetron cosputtering and characterized. Because of phonon-alloy disorder scattering within the solid solution, it is generally expected that the thermal conductivity will be several orders of magnitude lower than that of AlN and BN. A phonon gas model modified with a virtual crystal approximation (VCA) and phonon-alloy disorder scattering was created to validate and interpret the measurement results. Details are explained in the Section 7.

The measured data agrees with the phonon gas modeling results as shown in Figure 3a. The modeling results show that the $\kappa_\perp$ of an AlN film is 42.6 W m^{-1} K^{-1}, which is lower than

the $\kappa_\perp$ of single crystal bulk AlN due to phonon-boundary scattering.[34] The $\kappa_\perp$ is further reduced to 20.7 W m^{-1} K^{-1} by incorporating 1% of B into the cationic sublattice ($Al_{0.99}B_{0.01}N$) because of phonon-alloy disorder scattering. The $\kappa_\perp$ of $Al_{1-x}B_xN$ keeps reducing with x and reaches a minimum value of 4.6 W m^{-1} K^{-1} for $x = 0.2$. Device designers should account for this reduction of $\kappa_\perp$ with x to describe device self-heating. The mean value of the measured $\kappa_\perp$ of $Al_{0.82}B_{0.18}N$ is ∼15% lower than the modeling result. This is thought to be due to the lower crystalline quality of this film as compared to the other samples. X-ray diffraction (XRD) measurements show that the (0002) peak amplitude and full width at half-maximum (fwhm) of the $Al_{0.82}B_{0.18}N$ sample are 1 order of magnitude lower and 2 times broader, respectively, than those for other $Al_{1-x}B_xN$ samples, as depicted in Figure 3b. In addition, a (1001) peak is observed for the $Al_{0.82}B_{0.18}N$ sample. These XRD signatures indicate that the c-axis texture of the $Al_{0.82}B_{0.18}N$ film is relatively poor as compared to the other samples.

Figure 3c shows the E_2 (high) phonon frequency of $Al_{1-x}B_xN$ measured by Raman spectroscopy. The E_2 (high) phonon peak position exhibits a blue-shift as x increases. The shift in the phonon frequency agrees well (<2% error) with values calculated by the VCA thermal conductivity model described in the Section 7 (Figure 3d). This reflects that the VCA reasonably calculates the phonon dispersion of $Al_{1-x}B_xN$, including acoustic phonon branches that mainly contribute to the thermal conductivity. It should be noted that the E_2 (high) phonon peak could not be detected for $Al_{0.82}B_{0.18}N$, which is thought to be due to relatively poor c-axis texturing, also manifested in XRD and thermal conductivity (i.e., low $\kappa_\perp$) measurements.
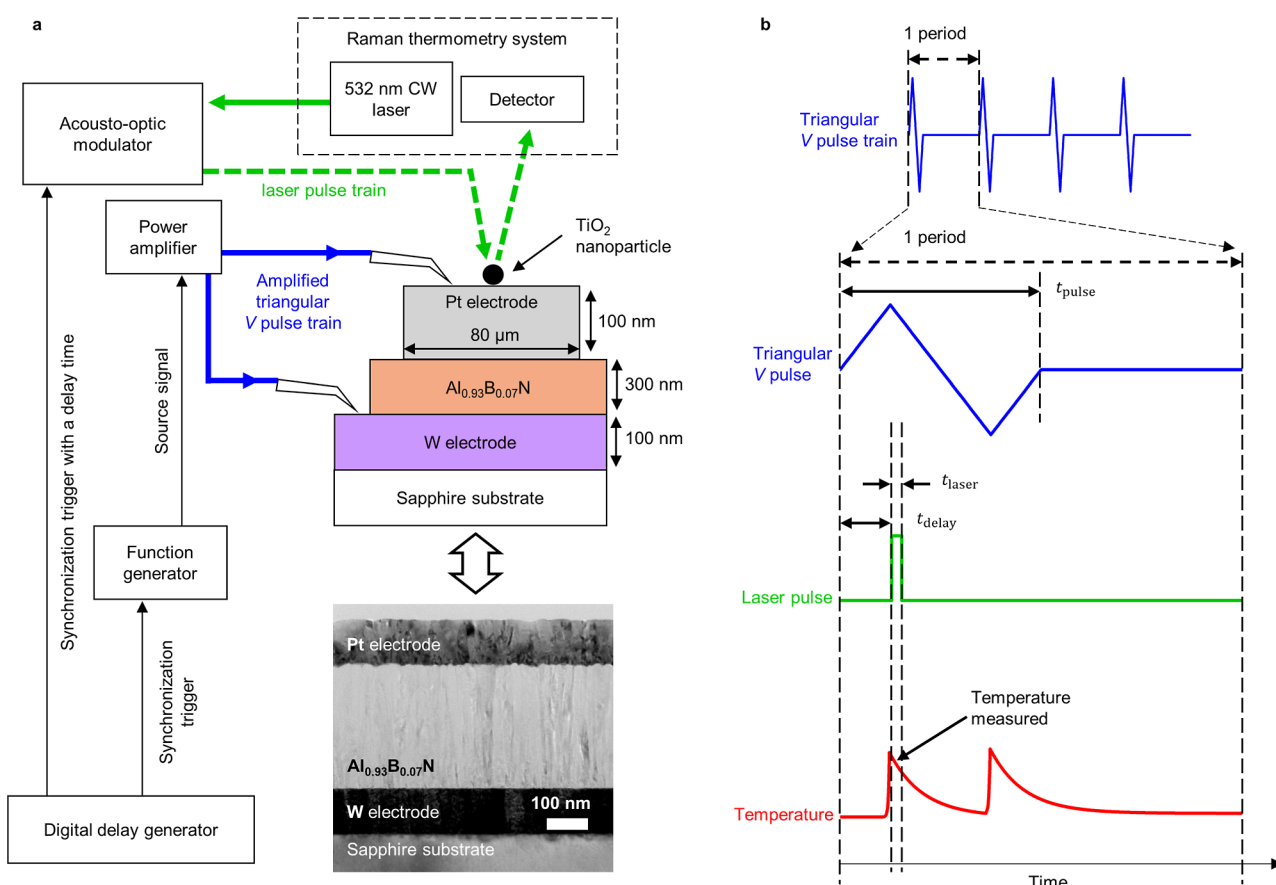
Figure 4. Transient temperature measurement system. (a) Schematic of the nanoparticle-assisted Raman thermometry measurement setup and a cross-sectional scanning transmission electron microscopy image of the MFM ($Pt/Al_{0.93}B_{0.07}N/W$) capacitor. (b) Synchronization between the triangular AC voltage pulse and the laser excitation pulse during transient Raman thermometry measurements to capture the transient thermal response of the device (red line at the bottom). The blue line (top) illustrates a periodic pulse train of a triangular AC voltage applied to the sample. A periodic Raman laser excitation with a pulse width of t_{laser} (green line) is synchronized with the triangular voltage train. The laser time delay (t_{delay}) is controlled to collect temperature information spanning an entire period of the triangular voltage pulse.

The thickness of the $Al_{1-x}B_xN$ layer of future FeRAM is expected to be less than 10 nm to keep the device operating voltage at a modest level. For example, switching the polarization with a voltage of 5 V requires the film thickness to be less than 10 nm because the E_c of $Al_{1-x}B_xN$ is larger than 5 MV/cm[33]. Since it is not obvious which x will be optimal for FeRAM at this time, the film thickness effect (i.e., phonon-boundary scattering) on $\kappa_\perp$ was evaluated for $Al_{1-x}B_xN$ films with an x of 0.07. The results in Figure 3e show that $\kappa_\perp$ decreases as the film thickness reduces due to an increase in the phonon-boundary scattering rate.

Stable operation under relatively high ambient temperature conditions is one of the most promising benefits of ferroelectric wurtzite nitrides.[9] TDTR measurements were performed to understand the temperature dependence of $\kappa_\perp$ for an $Al_{1-x}B_xN$ film with $x = 0.07$ and the results are shown in Figure 3f. The results show that $\kappa_\perp$ initially increases with temperature and plateaus for temperatures higher than 150 K. Beyond this temperature, phonon transport is mainly restricted by phonon-alloy disorder and phonon-boundary scattering effects instead of other scattering mechanisms, including phonon-Umklapp scattering. The two main scattering sources are the B-composition (x) and the thickness of the $Al_{1-x}B_xN$ layer, not the ambient temperature. Therefore, $\kappa_\perp$ is weakly temperature dependent within this temperature range. Figure 3g shows model predictions for the $\kappa_\perp$ of $Al_{0.93}B_{0.07}N$ with

three different thicknesses including a 5 nm case that is relevant to future FeRAM applications. Results indicate that $Al_{1-x}B_xN$ layers to be used in FeRAM devices with a thickness of less than 10 nm will possess a low ($\sim$1 W m^{-1} K^{-1}) and constant thermal conductivity above room temperature.

4. SELF-HEATING OF AN $AL_{0.93}B_{0.07}N$ MFM CAPACITOR

Nanoparticle-assisted micro-Raman thermometry was used to measure (i) the time-averaged temperature rise after the baseline temperature reaches a steady-state value (ΔT_{avg}) as well as (ii) the instantaneous peak temperature rise (ΔT_{peak}) of an $Al_{1-x}B_xN$ metal−ferroelectric−metal (MFM) capacitor. The MFM capacitor structure consists of: Pt top-electrode (100 nm)/$Al_{0.93}B_{0.07}N$ active layer (300 nm)/W bottom-electrode (100 nm)/sapphire substrate as shown in Figure 4a. While an alternating current (AC) triangular voltage (50−7000 Hz) was periodically applied to the MFM capacitor, ΔT_{avg} was measured with a 30 s data acquisition time (laser exposure) to achieve a reasonably high signal-to-noise ratio. On the other hand, the measurement of ΔT_{peak} requires a much shorter data acquisition time (e.g., 2 μs used in this work), and measurement needs to be done at the timing when the temperature reaches a peak value. To accomplish this while accumulating a sufficiently large amount of Raman scattered photons, the triangular AC voltage pulse applied to the MFM
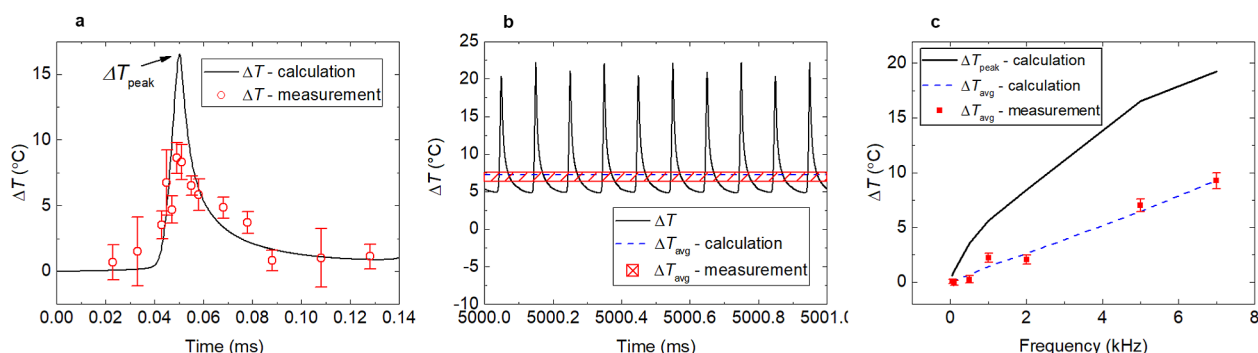
Figure 5. Characterization results of the top electrode temperature of an $Al_{0.93}B_{0.07}N$ MFM capacitor. (a) Transient Raman thermometry (open symbols) and thermal modeling results (black line) in response to 5 kHz AC triangular electric field operation. (b) The steady-state temperature rise of a MFM capacitor operating under 5 kHz continuous AC triangular electric field measured using Raman thermometry (red box patterned with diagonal lines) and calculated via thermal modeling (blue dashed line). (c) The instantaneous peak temperature rise (simulation—black solid line) and time-averaged temperature rise (simulation—blue dashed line and experimental values—red symbols) as a function of the operational frequency.
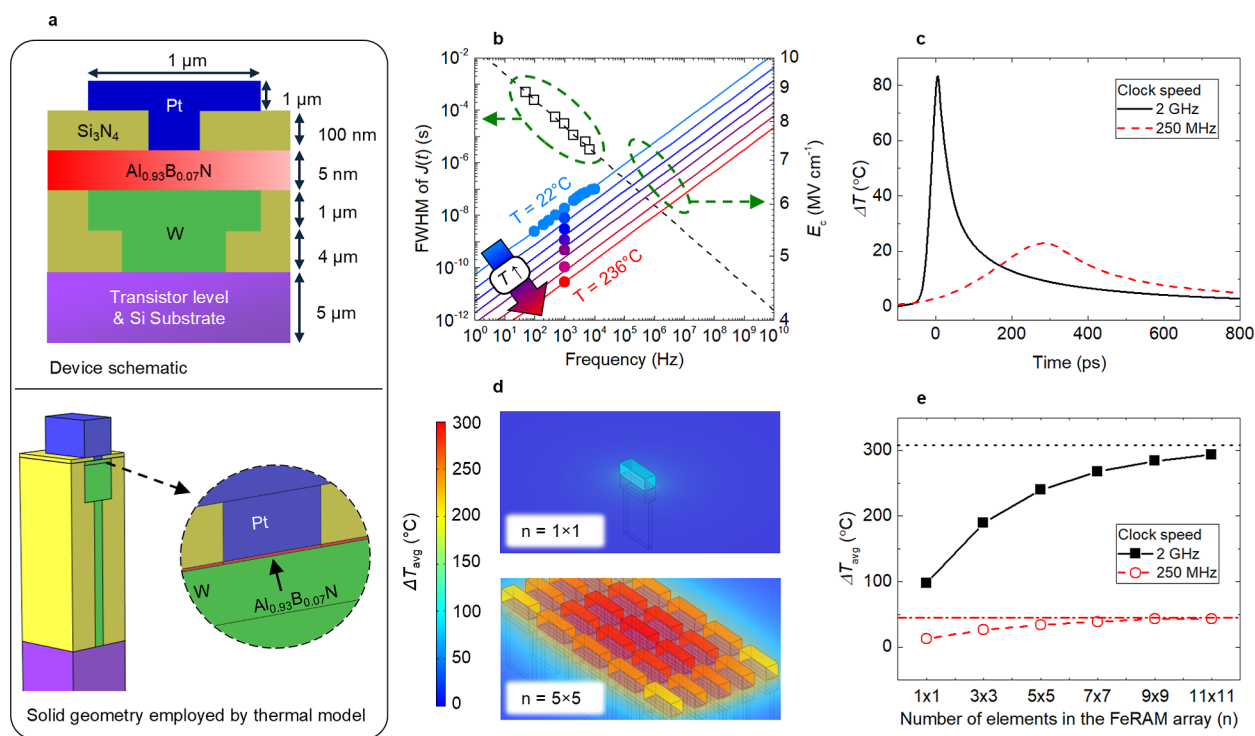

Figure 6. Simulation of high density FeRAM cell array. (a) Cross-sectional schematic of the hypothetical 1T1C FeRAM device structure that was investigated via thermal modeling. (b) The fwhm of the current density $[J(t)]$ and the coercive field (E_c) as a function of operational frequency and temperature. The dashed and solid lines are best fits to the measured fwhm (open squares) and E_c (solid circles), respectively, under various (relatively low) frequency levels. (c) The transient temperature excursion of the $Al_{0.93}B_{0.07}N$ layer in a 1T1C FeRAM device driven by a single polarization switching event under 2 GHz and 250 MHz clock speeds. (d) Thermal modeling results of a single isolated FeRAM device and a 5 × 5 device array for a clock speed of 2 GHz. (e) The impact of thermal crosstalk on the steady-state temperature rise (ΔT_{avg}) of device arrays with different sizes (i.e., number of bit-cells). The solid and opened symbols are simulation results for ΔT_{avg} for 2 GHz and 250 MHz clock speeds, respectively. The dotted black and red dash-dotted asymptote lines represent the calculated ΔT_{avg} values for 2 GHz and 250 MHz clock speeds, respectively when the number of arrayed devices (n) is infinity.

capacitor (1% duty cycle) and the laser pulse (t_{laser} = 2 μs) were synchronized and a periodic lock-in modulation scheme was used to increase the signal-to-noise ratio, as illustrated in Figure 4b. The laser pulse delay time (t_{delay}) was controlled to collect temperature information spanning over one period of the triangular voltage pulse. More details of the transient Raman thermometry measurements can be found in the Section 7.

A triangular bipolar AC electric field was applied to induce periodic polarization switching in the $Al_{0.93}B_{0.07}N$ layer. It should be noted that when a continuous AC electric field is applied, the volumetric heat generation rate, $g(t)$ is a periodic function where the power dissipation pulse exhibits a narrower width and higher amplitude for higher frequencies, as discussed in the Section 2. This means the transient thermal response of the device will be a superposition of a gradually increasing baseline temperature due to the accumulation of heat (which

eventually reaches a steady-state value) and a periodic instantaneous temperature rise that occurs during polarization switching, denoted as ΔT_{avg} and ΔT_{peak}, respectively. Figure 5a shows the transient temperature rise of the MFM capacitor (ΔT) during one period of an applied 5 kHz triangular bipolar electric field, measured via transient micro-Raman thermometry (open symbols). The experimental data are overlaid with calculation results from a device thermal model (black solid line). Details of the 3D finite element analysis (FEA) thermal model that calculates the thermal response of the MFM capacitor in response to the measured $g(t)$ can be found in the Section 7. The measured ΔT_{peak} values are lower because (i) each data point acquired via transient Raman thermometry is averaged over $t_{laser} = 2\ \mu s$ and (ii) heat dissipation through the needle probe in contact with the top electrode is not included in the thermal model. Figure 5b shows ΔT_{avg} analysis under a continuous 5 kHz triangular bipolar electric field. The transient temperature excursion (ΔT, black solid line) and the thermal modeling results of ΔT_{avg} (blue dashed line), as well as the steady-state Raman thermometry results of ΔT_{avg} (red box with diagonal line pattern) are shown in this plot. In Figure 5c, the measured/calculated ΔT_{avg} and the calculated ΔT_{peak} of the $Al_{0.93}B_{0.07}N$ MFM capacitor are compared for AC triangular electric field inputs with different frequencies. It is notable that both ΔT_{avg} and ΔT_{peak} increase with the operational frequency and ΔT_{peak} is significantly higher than ΔT_{avg} for a given frequency condition.

It was previously demonstrated that $Al_{1-x}B_xN$ exhibits outstanding data retention up to 200 °C.[12] Therefore, the modest self-heating behavior is not expected to negatively impact the retention of the memory state. However, this argument needs to be reassessed for high-density memory devices, as will be discussed in the next section.

5. SIMULATION OF SELF-HEATING IN A HYPOTHETICAL AL$_{0.93}$B$_{0.07}$N FERAM DEVICE ARRAY

The analysis of a single MFM capacitor indicates that more intense device self-heating may occur for higher frequency operation in terms of both ΔT_{avg} and the ΔT_{peak}. State-of-the-art random-access memory devices operate at clock speeds greater than 1 GHz.[19] This means a single FeRAM device can experience polarization switching at a frequency up to the clock speed of 1 GHz. A worst-case scenario in terms of self-heating will occur when data is continuously rewritten at this clock speed, where the continuous polarization switching maximizes the heat generation rate, $g(t)$. In addition, the ramp rate of the applied electric field is required to be higher than the clock speed as the memory should be written within one clock cycle (reversal of clock speed). As discussed before, the width and amplitude of $g(t)$ and ΔT_{peak} depend on the ramp rate and the GHz-level clock speed is expected to result in a significantly higher ΔT_{peak} than that shown in Figure 5c.

To quantify the self-heating behavior, a thermal model of a hypothetical one-transistor one-capacitor (1T1C) FeRAM based on an $Al_{0.93}B_{0.07}N$ layer was created as illustrated in Figure 6a (adapted based on a $Hf_{0.5}Zr_{0.5}O_2$ FeRAM device configuration reported in the literature[39,40]). The $Hf_{0.5}Zr_{0.5}O_2$ ferroelectric layer was replaced by a 5 nm thick $Al_{0.93}B_{0.07}N$ film so that the operating voltage can be kept below ~5 V. Modeling was performed for two different clock speeds: a 250 MHz case that represents space applications and a 2 GHz case that represents a modern CPU architecture. In terms of space

applications, the latest radiation-hardened microprocessors are RAD750 and GR740 with clock speeds of 200 and 250 MHz, respectively. The former was utilized in the James Webb space telescope in 2021 and the latter was released by the European space agency in 2020.

First, the transient thermal response of the 1T1C FeRAM device was analyzed when driven by a single polarization switching event. This contrasts to a worst-case scenario where polarization switching occurs during every clock cycle. The $g(t)$ for the 250 MHz and 2 GHz clock speeds could not be measured because of limitations associated with the experimental apparatus used in this work; instead, the $J(t)$ and $E(t)$ were calculated for $g(t)$. As discussed earlier, the width of $J(t)$ is determined by the electric field ramp rate. The peak amplitude and fwhm of $J(t)$ were extrapolated, assuming a linear relationship with the operational frequency, where measurement data were collected within a 50 Hz to 7 kHz range, as shown in Figure 6b. The extrapolation results for the fwhm of $J(t)$ are 193.7 and 24.2 ps for the 250 MHz and 2 GHz clock speeds, respectively. The peak amplitudes for the 250 MHz and 2 GHz clock speeds are 1.2 and 9.9 of 10^6 A cm^{-2}, respectively. It should be noted that there may be lower and upper bounds for the fwhm and peak amplitude, respectively due to an intrinsic limitation in the speed of polarization switching. Under such case, $g(t)$ will be less concentrated (i.e., the fwhm and peak amplitude of $J(t)$ will be wider and smaller, respectively) than the extrapolated value. Also, the clock speed has an upper limit due to the time required to charge the capacitor (RC time constant = $R \times C$, where R is the resistance and C is the capacitance[41]). If the RC time constant is longer than the period of the clock speed, the polarization may not be fully switched. The R includes both internal and parasitic resistances associated with the device test circuit. To evaluate the RC time constant of the hypothetical $Al_{0.93}B_{0.07}N$ FeRAM device, a previously reported parasitic specific contact resistance of $Al_{0.7}Sc_{0.3}N$ ($R_c \cdot A \sim 0.016\ \Omega\ cm^2$) and a total internal resistance for their measurement system (R_i = 104 Ω) were adopted,[42] where A is the contact area of the top electrode. From the measured P−E loops, the relative permittivity (ε_r) was determined to be 13.6. The C is $\varepsilon_r\varepsilon_0 \cdot A/t$, where ε_0 is the vacuum permittivity and t is thickness of the $Al_{0.93}B_{0.07}N$ layer. Then, the C and R_c are calculated as ~0.014 pF and 2.7 MΩ with $A = 6 \times 10^{-9}\ cm^2$ of the FeRAM model. Since the R_i mentioned above is negligible, the RC time constant for this geometry is ~38 ns, which is 2 orders of magnitude larger than the time period for 2 GHz operation. This indicates that a 2 orders of magnitude lower $R_c \cdot A$, than a currently achievable value[42] is necessary to accomplish a 2 GHz clock speed; it is likely that an alternative layout could mitigate this problem somewhat.

To estimate the E_c of the 5 nm thick $Al_{0.93}B_{0.07}N$ film for high frequency (250 MHz and 2 GHz) operation, the E_c of a 226 nm thick $Al_{0.93}B_{0.07}N$ film was measured using a triangular bipolar AC field with a frequency (f) range 100 Hz ~ 10 kHz. This sample adopts the same electrode scheme as the MFM capacitor tested in the Section 4 (i.e., 100 nm thick Pt top electrode and 100 nm thick W bottom electrode), but employs a different substrate (Si). A fitting model was built based on Ishibashi and Orihara's power-law dependence of E_c on the operational frequency[43,44] as described in eq 4.

$$E_c(f) = K(f \cdot [Hz^{-1}])^\beta \tag{4}$$

The K and β were determined to be 4.69 MV cm^{-1} and 0.033, respectively, by fitting eq 4 to the E_c values measured at room temperature (295.15 K). This value of β is comparable to those reported for a 100 μm thick 0.71Pb(Mg$_{1/3}$Nb$_{2/3}$)O$_3$-0.29PbTiO$_3$ film ($\beta = 0.04522$) and a 300 nm thick PZT film ($\beta = 0.05$), and smaller than a value reported for a 342 nm thick SBT film ($\beta = 0.12$).[44,45] Equation 4 predicts (extrapolates) the E_c to be 8.7 and 9.4 MV cm^{-1} under 250 MHz and 2 GHz clock speed operations, respectively. Note that the clock speed is twice of f because there are two triangular pulses during each cycle of a bipolar AC field.

The E_c of Al$_{.93}$B$_{0.07}$N is known to be a function of temperature.[6] Since $g(t)$ linearly scales with the E_c for a given $J(t)$, it is necessary to quantify the relation between E_c and temperature. The temperature dependence of E_c can be approximated using the Arrhenius equation (eq 5), where A_0 is a pre-exponential factor, E_a is the pseudoactivation energy for the polarization switching, and k_B is Boltzmann constant.

$$E_c(T) = A_0 \exp\left(\frac{E_a}{k_B T}\right) \tag{5}$$

The E_c and P_r of the 226 nm thick Al$_{0.93}$B$_{0.07}$N capacitor were measured at $f = 1$ kHz for a temperature range of 22−236 °C. The E_c decreased with temperature as shown in Figure 6b. By fitting the measurement results to eq 5, the E_a was determined to be 15.5 meV. To express E_c as a function of both f and T, eq 4 (at 295.15 K) and eq 5 were combined such that E_c can be approximated as eq 6.

$$E_c(f, T) = K f^\beta \exp\left[\left(\frac{E_a}{k_B}\right)\left(\frac{1}{T} - \frac{1}{295.15\ \text{K}}\right)\right] \tag{6}$$

P_r is also expected to be a function of temperature such that $J(t)$ is temperature dependent according to eq 2. The remanent polarization in the wurtzite ferroelectric materials decreases extremely slowly as a function of temperature, since there is no known Curie temperature before decomposition or melting. In summary, the aforementioned relations for E_c and $J(t)$ were used to calculate $g(t)$, which is a crucial input for the thermal modeling, as a function of both frequency and temperature. Figure 6c shows the transient thermal response of a 1T1C FeRAM device in response to the $g(t)$ determined above for a single 250 MHz or 2 GHz triangular electric field pulse input. As discussed in the Section 3, the $\kappa_\perp$ of a 5 nm thick Al$_{0.93}$B$_{0.07}$N layer is predicted to be ~1 W m^{-1} K^{-1}. For switching at 2 GHz, the low $\kappa_\perp$ and the large peak amplitude of $g(t)$ lead to a large instantaneous ΔT_{peak} that reaches up to ~83 °C, which is an order of magnitude higher than the ΔT_{peak} for the MFM device analyzed in the Section 4. On the other hand, ΔT_{peak} under 250 MHz operation is ~23 °C.

Next, the impact of thermal crosstalk on the self-heating of a 2D FeRAM cell-array was interrogated. Thermal crosstalk refers to the amplified self-heating in one section of a high-density device array (as compared to the case of a single isolated device) due to the generation of heat in a nearby section; the adjacent heat generation forms a periodic thermal boundary condition that hinders lateral spreading of the generated heat.[46] To quantify this effect in an Al$_{0.93}$B$_{0.07}$N FeRAM array, the 1T1C FeRAM device model was duplicated to form a periodic cell-array. The steady-state ΔT_{avg} of the hottest center bit-cell was calculated for several cell array sizes for the 250 MHz and 2 GHz clock speeds, as shown in Figure

6d. Each bit-cell unit is assumed to have an area of 1 μm × 3 μm, and the spacing between them is presumed to be 1 μm. The worst-case scenario of device self-heating is assumed, where data writing (i.e., polarization switching) occurs every single clock cycle to evaluate the highest possible ΔT_{avg}. Figure 6e shows that ΔT_{avg} increases with the number of cells in an array and can reach up to ~293 °C, which is ~3 times higher than that for a single element at the same clock speed of 2 GHz. Although wurtzite Al$_{0.93}$B$_{0.07}$N is known to be thermally stable, high temperature operation can sometimes be undesirable in terms of device reliability. The electrical breakdown field of Al$_{0.93}$B$_{0.07}$N was reported to reduce slowly with temperature.[6] In addition, it was reported that the leakage current flowing through a 15 nm thin Al$_{0.93}$B$_{0.07}$N layer increases at high temperatures.[47] This will exacerbate device self-heating via the increase in the Joule heating. Finally, the ferroelectric fatigue rate of Al$_{0.93}$B$_{0.07}$N was shown to increase with temperature. For instance, the number of polarization switching cycles resulting in fatigue failure was shown to reduce to ~16% when the temperature is increased from room temperature to 200 °C.[48] On the other hand, the ΔT_{avg} for a clock speed of 250 MHz is ~43 °C because g_{avg} and the amplitude of $g(t)$ are only ~12% of those for 2 GHz operation. The ΔT_{peak} under the 250 MHz operation is ~23 °C, which is a manageable temperature given the high temperature stability of wurtzite ferroelectric materials.[12] It should be noted that these results represent those for a worst-case scenario and the actual thermal response of a real FeRAM device will depend on several design factors including the bit-cell unit size, the distance between them,[46] the ramp rate of the electric pulse input, and the actual data rewriting rate. For FeRAM technologies based on AlN solid solutions to be used in applications that require GHz-level high speed computation, electro-thermal codesign techniques (such as high thermal conductivity substrate heterogeneous integration)[49] may need to be employed to mitigate device self-heating.

6. CONCLUSIONS

The thermal conductivity of Al$_{1-x}$B$_x$N thin films was determined as a function of B-composition, film thickness, and ambient temperature using TDTR. The measurement results were validated using a model based on Callaway's phonon gas theory augmented by a virtual crystal approximation (VCA) to account for phonon-alloy disorder scattering. The transient and steady-state self-heating in an Al$_{0.93}$B$_{0.07}$N metal−ferroelectric−metal (MFM) capacitor caused by polarization switching was characterized using nanoparticle-assisted Raman thermometry. The experimental results were validated using a finite element analysis (FEA) device thermal model that employs the measured thermal properties and the heat generation rate determined from ferroelectric hysteresis measurements. It was found that more intense self-heating occurs with an increase in the operational frequency because the heat generation rate becomes more concentrated within a shorter time period. Simulation results for hypothetical high-density FeRAM arrays show that thermal crosstalk among bit-cells further exacerbates device self-heating. The experimental and simulation results from this work reveal that the low thermal conductivity (for sub-10 nm thick films) and the large amount of heat generated during polarization switching (due to large E_c and P_r) may render Al$_{1-x}$B$_x$N-based FeRAM devices prone to thermal reliability issues, for reversal at GHz-level clock speeds. However, the

amount of heating drops rapidly as the frequency for polarization reversal is reduced.

7. METHODS

7.1. Film Growth, Characterization, and Device Fabrication. $Al_{1-x}B_xN$ thin films were deposited on sapphire substrates at 300 °C via reactive magnetron cosputtering, using argon and nitrogen as the process gases and 2″ diameter Al (99.999% purity, Kurt J. Lesker) and 2″ diameter BN (99.5% purity, Plasmaterials) as the cathodes. Al was sputtered using pulsed DC excitation (100 kHz and 1.53 μs pulse width) at a time averaged power of 250 W. BN was sputtered using radio frequency (RF) excitation at a time averaged power of 0−200 W depending on the targeted $Al_{1-x}B_xN$ composition. The chamber base pressure was $\sim 5 \times 10^{-8}$ Torr. The films were grown at a pressure of 2 mTorr.

Metal−ferroelectric−metal, MFM, capacitors were fabricated in the same chamber. The W bottom electrode and the top Pt electrode were sputtered in situ. As described above, a 300 and 226 nm thick $Al_{0.93}B_{0.07}N$ layers were deposited on the W bottom electrode [100 nm] grown on a sapphire substrate and Si substrate, respectively, at 300 °C.

The film structural parameters were evaluated using a Malvern Panalytical Empyrean X-ray diffractometer (XRD) equipped with a Bragg−Brentano^{HD} incident optics and a PIXcel3D solid state detector with programmable antiscatter slit (PASS) diffracted beam optics. Symmetric $\theta-2\theta$ scans in the Bragg−Brentano geometry were used to assess phase purity and film orientation.

The $Al_{0.93}B_{0.07}N$ crystal structure and orientation were imaged using a Titan^{3TM} G2 60−300 STEM system with a 0.7 Å of resolution. The samples were prepared with a focused ion beam milling system.

7.2. Thermal Property Measurement. TDTR was used to characterize the $Al_{1-x}B_xN$ thin films. TDTR is a laser-based pump−probe method where the temperature rise of the specimen in response to pump laser heating is detected using a probe laser reflected from the sample surface.[50] The thermoreflectance effect can be described as

$$\Delta R \approx C_{TR} \Delta T$$

where R is the reflectance of a metal transducer deposited on the sample surface, C_{TR} is the thermoreflectance coefficient, and ΔT is the temperature rise. The focused pump and probe beam spot diameters (18 and 9.5 μm, respectively) were measured using a scanning-slit optical beam profiler (Thorlabs BP2089-VIS). The TDTR signal represents the transient temperature excursion of a sample surface after the pump laser pulse hits the surface, leading to optical heating of the metal transducer. A mechanical delay stage was used to manipulate the timing of the incident probe pulse and the transient thermal response to the pump laser heating was captured. The temperature excursion data was fit to a transient heat diffusion model to extract the $\kappa_\perp$. Thermal properties other than $\kappa_\perp$ that were used in the model are summarized in Table 1. Flint FL2-12 (Light Conversion) was used to generate a 1035 nm pulsed laser, and a part of this laser light was converted to a 518 nm pulsed laser by passing through a BiB_3O_6 crystal that results in second-harmonic generation. The 1035 nm laser was used as a probe and the 518 nm laser was used as the pump. The pump laser pulse was modulated with

a frequency of 7 MHz using an electro-optic modulator and detected using a lock-in amplifier (Zurich Instruments UHFLI)

Aluminum (Al) metal transducers were deposited on the $Al_{1-x}B_xN$ sample surfaces to perform the TDTR measurements since Al offers a C_{TR} appropriate for the 1035 nm probe laser.[51] A transducer thickness of 80 nm was selected to maximize the signal-to-noise ratio and the measurement sensitivity to the $Al_{1-x}B_xN$ thermal conductivity. Deposition of the Al metal transducer was performed using electron beam evaporation. Aluminum (purity 99.999%) metal pieces were placed in a water-cooled crucible centered under the electron beam. Thechamber base pressure was 10^{-8} Torr, and the working distance between the metal source and the substrate was 60 cm. Samples were fastened to the puck using double sided tape and regions of each sample surface were masked using Kapton tape. The deposition rate and film thickness were measured in situ using a quartz crystal microbalance (QCM). The targeted deposition thickness was 80 nm and the deposition rate was 7 nm/min. Bare, c-plane, single side polished sapphire substrates (10 × 10 mm) were loaded in the deposition chamber. The resulting metal films served as witness samples for the transducer films.

The film density, thickness, and roughness of the witness samples were estimated by X-ray reflectivity (XRR). Fitting of the XRR data determined that the Al metal transducers were 77 nm thickness.

7.3. Device Thermal Imaging. Nanoparticle-assisted Raman thermometry[23] was used to perform in situ temperature measurement of the $Al_{1-x}B_xN$ MFM capacitors during polarization switching. Because the top metal electrode hinders acquisition of a Raman signal, anatase TiO_2 nanoparticles (99.98% purity) were deposited onto the device, serving as surface temperature probes. The size of the nanoparticles (or nanoparticle agglomerates), which dictates the spatial resolution of this method, ranged from 0.2 to 1 μm. During device operation, the peak shift of the E_g mode of the TiO_2 nanoparticles was used to deduce the surface temperature rise. The relationship between temperature and the E_g phonon frequency (~ 143 cm^{-1} at room temperature) of the TiO_2 agreed with reported results.[57] A Horiba LabRAM HR Evolution Raman microscope equipped with a 532 nm laser, a grating with 1800 grooves/mm, and a long working distance 50× objective lens was used for these measurements. The incident laser power was adjusted (<0.5 mW) to prevent laser-induced heating of the top electrode and nano-particles. For time-averaged temperature (ΔT_{avg}) measurements, a continuous wave (CW) laser was used without modulation and synchronization. The ΔT_{avg} data were collected over a 30 s acquisition time while a continuous triangular AC voltage was applied to the MFM capacitor for polarization switching. For transient temperature measurements, the CW laser was modulated into a 2 μs width square pulse train using an acousto-optic modulator (AA Opto-electronic MODA 180). For synchronization (Figure 4b), the voltage pulses for polarization switching were also modulated into a 200 μs width triangular pulse train using a function generator (Stanford Research System DS345). The acousto-optic modulator and function generator were synchronized by a digital delay generator (Stanford Research System DG535), which also controls the time delay between a voltage pulse and a laser pulse (t_{delay} in Figure 4b). The synchronized laser and voltage pulses were generated using a 50 Hz repetition rate. More details of the transient Raman thermometry setup can be found in ref 58. After data acquisition during a prolonged time duration, the top electrode of some of the MFM capacitors underwent visible degradation (near the edge of the electrode). This degradation phenomenon caused by electric field concentration has been reported for $Al_{0.93}B_{0.07}N$ MFM capacitor in a previous work.[48]

7.4. Thermal Conductivity Modeling. The measured $\kappa_\perp$ was evaluated using Callaway's phonon gas model[35−37] modified with a virtual crystal approximation (VCA) to account for the effect of phonon-alloy disorder scattering.[38] VCA assumes that the $Al_{1-x}B_xN$ solid solution possesses an ordered virtual crystal structure with phononic properties that are weighted averages of wurtzite AlN and wurtzite BN based on the composition, x. In the VCA adopted here, the overall dispersion relationship of $Al_{1-x}B_xN$ phonon energy (ω)

Table 1. Thermal Properties Adopted for the TDTR Data Fitting Process^a

	Al	$Al_{1-x}B_xN$	sapphire
c_v (10^6 J m^{-3} K)	ref 52	interpolation with refs 53 and 54	ref 55
$\kappa_\perp$ (W m^{-1} K^{-1})	ref 56	this work	
$\kappa\|$ (W m^{-1} K^{-1})		this work (model calculation)	

$^a c_v$ is the volumetric heat capacity, $\kappa_\perp$ is the cross-plane thermal conductivity (along the c-axis), and $\kappa_\parallel$ is the in-plane thermal conductivity (across the c-plane).

was calculated as $\omega_{Al_{1-x}B_xN} = \left(\frac{x}{\omega_{BN}^2} + \frac{1-x}{\omega_{AlN}^2}\right)^{-1/2}$. The ω_{BN} and ω_{AlN} values employed here are first-principles calculation results reported elsewhere.[59,60] The E_2 (high) phonon energy calculated here shows less than 2% error compared to the measured E_2 (high) phonon energy by Raman spectroscopy for x = 0, 0.05, 0.07, 0.012 (see Section 3). This reflects that the ω calculation is valid for $Al_{1-x}B_xN$ within the range of x studied. In this model, $\kappa_\perp$ is calculated for acoustic phonon branches (i), as shown in eqs 7 and 8

$$\kappa_\perp = \sum_i \kappa_i \tag{7}$$

$$\kappa_i = \frac{k_B^4}{6\pi^2\hbar^3 v_i}T^3 \times$$

$$\left[\int_0^{\theta_{D,i}/T} X^4 \frac{e^X}{(e^X-1)^2}\tau_i^C\, dX + \frac{\int_0^{\frac{\theta_{D,i}}{T}} X^4 \frac{e^X}{(e^X-1)^2}\frac{\tau_i^C}{\tau_i^N}\, dX}{\int_0^{\frac{\theta_{D,i}}{T}} X^4 \frac{e^X}{(e^X-1)^2}\frac{\tau_i^C}{\tau_i^N\tau_i^R}\, dX}\right] \tag{8}$$

where k_B is Boltzmann's constant, $\hbar$ is Planck's constant, T is temperature, $\omega_i(q)$ is the phonon frequency for a given branch as a function of the wavenumber (q), v_i is the sound velocity defined as $d\omega_i(q)/dq$, $\theta_{D,i}$ is the Debye temperature defined as $\hbar\omega_{D,i}/k_B$, and $X = \hbar\omega_i/k_BT$. As the cross-plane thermal conductivity is of primary interest, the phonon dispersion relationship used in the calculation only accounts for phonon branches that propagate parallel to the c-axis, as reported elsewhere.[54,60] τ_i^R is the resistive phonon relaxation time considering phonon-Umklapp (τ_iU), phonon-boundary (τ_i^B), phonon-point defect (τ_i^P), and phonon-alloy disorder (τ_i^A) scattering processes. The normal phonon scattering time for nonresistive scattering processes is τ_i^N. The effective phonon scattering rate ($1/\tau_i^C$) accounting for both resistive and nonresistive scattering processes is calculated based on Matthiessen's rule as shown in eqs 9 and 10.

$$\frac{1}{\tau_i^R} = \frac{1}{\tau_i^U} + \frac{1}{\tau_i^B} + \frac{1}{\tau_i^P} + \frac{1}{\tau_i^A} \tag{9}$$

$$\frac{1}{\tau_i^C} = \frac{1}{\tau_i^R} + \frac{1}{\tau_i^N} \tag{10}$$

The phonon relaxation times were calculated according to eqs 11−14.

Phonon-Umklapp scattering (i.e., the resistive three-phonon scattering process) plays a major role in reducing the thermal conductivity at high temperatures because of the increased scattering rate. The phonon-Umklapp scattering rate for the ith phonon branch is expressed as

$$\frac{1}{\tau_i^U} = \frac{\hbar\gamma_i^2\omega_i^2 T}{Mv_i^2\theta_D^i}e^{-\frac{\theta_{D,i}}{3T}} \tag{11}$$

where γ_i is the Grüneisen parameter for the ith phonon branch and M is the average atomic mass [e.g., for AlN, $M = (26.982 + 14.007)/2$ g/mol].

The normal phonon scattering rate is determined by the following expression with a set of coefficients (a, b) and the average atomic volume V_o (=M × density). The sets of coefficients are (2, 1) for the longitudinal acoustic phonon branch and (1, 1) for the transverse mode, respectively.[37]

$$\frac{1}{\tau_i^N} = \left(\frac{k_B}{\hbar}\right)^{a+b}\frac{\hbar\gamma_i^2(V_o)^{\frac{a+b-2}{3}}}{Mv_i^{a+b}}\left(\frac{\hbar\omega}{k_BT}\right)^a T^{a+b} \tag{12}$$

where V_o is the average atomic volume (M × density). As γ_i of $Al_{1-x}B_xN$ alloys has not been reported, $1/\tau_i^U$ and $1/\tau_i^N$ of $Al_{1-x}B_xN$ were found by applying Vegard's law to those of wurtzite AlN and BN.

The phonon-boundary scattering time is defined as the lifetime of acoustic phonons propagating across the thickness (d) of the sample at the sound velocity (v_i).

$$\frac{1}{\tau_i^B} = \frac{v_i}{d} \tag{13}$$

With regards to phonon-point defect scattering, both impurity elements and vacancies are treated as point defects. The scattering time was calculated as

$$\frac{1}{\tau_i^P} = \frac{V_o}{4\pi v_i^3}\omega_i^4\Gamma_i^P \tag{14}$$

where Γ_i^P is the mass-fluctuation phonon-scattering parameter derived from unintended impurities and the vacancy concentration, that is described in eq 15, as suggested by Klemens[61]

$$\Gamma_i^P = \sum_j f_j\left\{\left(\frac{m_j - M}{M}\right)^2 + 8\gamma_i^2(1+Q)^2\left(\frac{r_j - r_o}{r_o}\right)^2\right\} \tag{15}$$

where f_j and m_j are the mole fraction and atomic mass of the jth impurity, and r_j and r_o are the atomic radius of the jth impurity and the standard atomic radius of the host crystal ($Al_{1-x}B_xN$), respectively. AlN and BN are largely covalently bonded materials with 40% and 22% ionic characters, respectively, based on the Pauling electronegativity difference. Here, covalent radii were adopted to represent r_j and r_o. The experimentally determined bond lengths of AlN (1.899 Å) and BN (1.571 Å) are comparable with the calculated result (1.92 Å for AlN and 1.55 Å for BN) based on the covalent radius.[62] Q is a number calculated based on the difference of anharmonicity between bonds of impurities and the host crystal.[61] In this work, the Γ_i^P parameter was not calculated due to the limited information of f_j for each element and vacancy; instead it was used as a fitting parameter.

The calculation process for phonon-alloy disorder scattering is similar to that for impurity scattering; however, the mass-fluctuation phonon-scattering parameter (Γ_i^A) was calculated such that atomic mass and size contribute to the phonon-alloy disorder scattering rate. In the virtual crystal of $Al_{1-x}B_xN$, the phonon energy dispersion is defined based on the assumption that there is long-range order for the cation sublattice. However, $Al_{1-x}B_xN$ is a solid-solution where both Al and B atoms contribute to the disorder in the virtual crystal. Therefore, Γ_i^A and τ_i^A are expressed with $Q = 4.2$[61] in eqs 16 and 17 where l represents the elements, Al and B.

$$\frac{1}{\tau_i^A} = \frac{V_o}{4\pi v_i^3}\omega_i^4\Gamma_i^A \tag{16}$$

$$\Gamma_i^A = \sum_l f_l\left\{\left(\frac{m_l - M}{M}\right)^2 + 8\gamma_i^2(1+Q)^2\left(\frac{r_l - r_o}{r_o}\right)^2\right\}$$

$$= f_{Al}\left\{\left(\frac{m_{Al} - M}{M}\right)^2 + 8\gamma_i^2(1+Q)^2\left(\frac{r_{Al} - r_o}{r_o}\right)^2\right\}$$

$$+ f_B\left\{\left(\frac{m_B - M}{M}\right)^2 + 8\gamma_i^2(1+Q)^2\left(\frac{r_B - r_o}{r_o}\right)^2\right\} \tag{17}$$

Finally, $\kappa_\perp$ was found according to eqs 7 and 8 with the phonon scattering times calculated from eqs 9−17. All parameters used in the thermal conductivity model are summarized in Table 2.

The γ_i and Γ_i^P were used as fitting parameters. Those for AlN were first found through two fitting processes: (1) fitting the calculated $\kappa_\perp$ of pure bulk ($\Gamma_i^P = 0$) wurtzite AlN to literature values of 300−320 W m^{-1} K^{-1} (refs 63 and 64) and (2) fitting the measured $\kappa_\perp$ of the 400 nm thick, unintentionally doped AlN layer sample to the calculation result where the γ_i and Γ_i^P were fitting parameters.[62,63] The γ_i parameters for transverse (γ_T) and longitudinal (γ_L) acoustic phonons of AlN were found to be 0.30 ± 0.10 and 0.75 ± 0.27, respectively,

Table 2. Parameters Used in the Thermal Conductivity Model[a]

		AlN	BN
transverse acoustic phonon	γ	0.30 ± 0.10	0.32 ± 0.05
	θ_D (K)	236	482
	v_i (10^3 m s^{-1})	4.2–5.5	6.2–10
longitudinal acoustic phonon	γ	0.75 ± 0.27	0.99 ± 0.37
	θ_D (K)	459	870
	v_i (10^3 m s^{-1})	9–10.2	13.2–17.5
	Al	B	N
m	26.982	10.806	14.007
r (Å)	1.21	0.84	0.71

[a]γ is the Grüneisen parameter (found in this research), θ_D is the Debye temperature (refs 59 and 60), v_i is sound velocity (refs 59 and 60), m is the atomic weight, and r is the ionic radii (ref 62).

which are consistent with previously reported data.[38] The Γ_i^P was determined to be 0.0126 ± 0.0026. This result is comparable to the reported Γ_i^P value of 0.01 for a 394 nm AlN layer sample,[65] grown under similar conditions (on a sapphire substrate using a reactive magnetron sputtering system). Finally, the γ_T and γ_L of BN were determined to be 0.32 ± 0.05 and 0.99 ± 0.37, respectively, through two data fitting processes: (1) fitting the measured $\kappa_\perp$ of 400 nm thick $Al_{1-x}B_xN$ layer samples to the model calculation based on γ_i and Γ_i^P of AlN found above, and (2) fitting the calculated $\kappa_\perp$ of a pure bulk wurtzite BN to the literature values of 600−1150 W m^{-1} K^{-1} from ab initio calculations.[66,67] Using these parameters, the $\kappa_\perp$ of all other $Al_{1-x}B_xN$ layer samples were calculated and compared with the measured $\kappa_\perp$, as shown in Figure 3.

7.5. Device Thermal Modeling. In order to computationally evaluate the temperature rise of MFM capacitors and FeRAM devices, 3D finite element analysis (FEA) thermal models were constructed using COMSOL Multiphysics. In the MFM device analysis, the measured $g(t)$ was employed as a heat source in the active $(Al_{0.93}B_{0.07}N)$ layer. For the hypothetical 1T1C FeRAM simulation, a calculated $g(t)$ was used. A natural heat convection boundary condition was applied to the top surface and side walls of the devices.[68,69] For the MFM capacitor simulation, the temperature boundary condition for the bottom surface was room temperature, similar to the experimental setup. For the 1T1C FeRAM device simulation, the bottom surface temperature was assumed to be 50 °C, to account for the elevated ambient temperature caused by the transistor-level below the capacitor devices.

AUTHOR INFORMATION

Corresponding Authors

Sukwon Choi − *Department of Mechanical Engineering, The Pennsylvania State University, University Park, Pennsylvania 16802, United States;* ⓘ orcid.org/0000-0002-3664-1542; Email: sukwon.choi@psu.edu

Susan E. Trolier-McKinstry − *Department of Materials Science and Engineering, The Pennsylvania State University, University Park, Pennsylvania 16802, United States;* ⓘ orcid.org/0000-0002-7267-9281; Email: set1@psu.edu

Authors

Kyuhwe Kang − *Department of Mechanical Engineering, The Pennsylvania State University, University Park, Pennsylvania 16802, United States*

Joseph A. Casamento − *Department of Materials Science and Engineering, The Pennsylvania State University, University Park, Pennsylvania 16802, United States*

Daniel C. Shoemaker − *Department of Mechanical Engineering, The Pennsylvania State University, University Park, Pennsylvania 16802, United States*

Yiwen Song − *Department of Mechanical Engineering, The Pennsylvania State University, University Park, Pennsylvania 16802, United States*

Erdem Z. Ozdemir − *Department of Materials Science and Engineering, The Pennsylvania State University, University Park, Pennsylvania 16802, United States*

Nathaniel S. McIlwaine − *Department of Materials Science and Engineering, The Pennsylvania State University, University Park, Pennsylvania 16802, United States*

Jon-Paul Maria − *Department of Materials Science and Engineering, The Pennsylvania State University, University Park, Pennsylvania 16802, United States*

Complete contact information is available at:
https://pubs.acs.org/10.1021/acsami.4c14022

Notes

The authors declare no competing financial interest.

REFERENCES

(1) Kneissl, M.; Seong, T. Y.; Han, J.; Amano, H. The Emergence and Prospects of Deep-Ultraviolet Light-Emitting Diode Technologies. *Nat. Photonics* **2019**, *13* (4), 233−244.

(2) Tsao, J. Y.; Chowdhury, S.; Hollis, M. A.; Jena, D.; Johnson, N. M.; Jones, K. A.; Kaplar, R. J.; Rajan, S.; Van de Walle, C. G.; Bellotti, E.; Chua, C. L.; Collazo, R.; Coltrin, M. E.; Cooper, J. A.; Evans, K. R.; Graham, S.; Grotjohn, T. A.; Heller, E. R.; Higashiwaki, M.; Islam, M. S.; Juodawlkis, P. W.; Khan, M. A.; Koehler, A. D.; Leach, J. H.; Mishra, U. K.; Nemanich, R. J.; Pilawa-Podgurski, R. C. N.; Shealy, J. B.; Sitar, Z.; Tadjer, M. J.; Witulski, A. F.; Wraback, M.; Simmons, J. A. Ultrawide-Bandgap Semiconductors: Research Opportunities and Challenges. *Adv. Electron. Mater.* **2018**, *4* (1), 1600501.

(3) Akiyama, M.; Kamohara, T.; Kano, K.; Teshigahara, A.; Takeuchi, Y.; Kawahara, N. Enhancement of Piezoelectric Response in Scandium Aluminum Nitride Alloy Thin Films Prepared by Dual Reactive Cosputtering. *Adv. Mater.* **2009**, *21* (5), 593−596.

(4) Piazza, G.; Felmetsger, V.; Muralt, P.; Olsson, R. H.; Ruby, R. Piezoelectric Aluminum Nitride Thin Films for Microelectromechanical Systems. *MRS Bull.* **2012**, *37* (11), 1051−1061.

(5) Fichtner, S.; Wolff, N.; Lofink, F.; Kienle, L.; Wagner, B. AlScN: A III–V Semiconductor Based Ferroelectric. *J. Appl. Phys.* **2019**, *125* (11), 114103.

(6) Zhu, W.; Hayden, J.; He, F.; Yang, J. I.; Tipsawat, P.; Hossain, M. D.; Maria, J. P.; Trolier-McKinstry, S. Strongly Temperature Dependent Ferroelectric Switching in AlN, Al$_{1-X}$Sc$_X$N, and Al$_{1-X}$B$_X$N Thin Films. *Appl. Phys. Lett.* **2021**, *119* (6), 062901.

(7) Casamento, J.; Baksa, S. M.; Behrendt, D.; Calderon, S.; Goodling, D.; Hayden, J.; He, F.; Jacques, L.; Lee, S. H.; Smith, W.; Suceava, A.; Tran, Q.; Zheng, X.; Zu, R.; Beechem, T.; Dabo, I.; Dickey, E. C.; Esteves, G.; Gopalan, V.; Henry, M. D.; Ihlefeld, J. F.; Jackson, T. N.; Kalinin, S. V.; Kelley, K. P.; Liu, Y.; Rappe, A. M.; Redwing, J.; Trolier-McKinstry, S.; Maria, J. P. Perspectives and Progress on Wurtzite Ferroelectrics: Synthesis, Characterization, Theory, and Device Applications. *Appl. Phys. Lett.* **2024**, *124* (8), 080501.

(8) Calderon, S.; Hayden, J.; Baksa, S. M.; Tzou, W.; Trolier-Mckinstry, S.; Dabo, I.; Maria, J.-P.; Dickey, E. C. Atomic-Scale Polarization Switching in Wurtzite. *Ferroelectrics* **2023**, *380*, 1034−1038.

(9) Wang, P.; Wang, D.; Mondal, S.; Hu, M.; Liu, J.; Mi, Z. Dawn of Nitride Ferroelectric Semiconductors: From Materials to Devices. *Semicond. Sci. Technol.* **2023**, *38* (4), 043002.

(10) Fenouillet-Beranger, C.; Mathieu, B.; Previtali, B.; Samson, M.-P.; Rambal, N.; Benevent, V.; Kerdiles, S. New Insights on Bottom Layer Thermal Stability and Laser Annealing Promises for High Performance 3D VLSI. In *2014 IEEE International Electron Devices Meeting; San Francisco*, 2014, pp 27.5.1−27.5.4.

(11) Cavalcante, C.; Fenouillet-Beranger, C.; Batude, P.; Garros, X.; Federspiel, X.; Lacord, J. 28nm FDSOI CMOS Technology (FEOL and BEOL) Thermal stability for 3D Sequential Integration: Yield and Reliability Analysis. In *2020; IEEE Symposium on VLSI Technology; Honolulu*, 2020, pp 1−2.

(12) Zhu, W.; He, F.; Hayden, J.; Yang, J. I.; Tipsawat, P.; Maria, J. P.; Trolier-McKinstry, S. Exceptional High Temperature Retention in Al$_{0.93}$B$_{0.07}$N Films. *Appl. Phys. Lett.* **2023**, *122* (24), 242902.

(13) Islam, M. R.; Wolff, N.; Yassine, M.; Schönweger, G.; Christian, B.; Kohlstedt, H.; Ambacher, O.; Lofink, F.; Kienle, L.; Fichtner, S. On the Exceptional Temperature Stability of Ferroelectric Al$_{1-X}$Sc$_X$N Thin Films. *Appl. Phys. Lett.* **2021**, *118* (23), 232905.

(14) Rubat du Merac, M. Transparent Ceramics: Materials, Processing, Properties and Applications. *Transparent Ceramics: Materials, Processing, Properties and Applications*; Elsevier, 2021; Vol. 1, pp 399−423.

(15) Siegel, A.; Parlinski, K.; Wdowik, U. D. Ab Initio Calculation of Structural Phase Transitions in AlN Crystal. *Phys. Rev. B:Condens. Matter Mater. Phys.* **2006**, *74* (10), 104116.

(16) Schmerler, S.; Kortus, J. Ab Initio Study of AlN: Anisotropic Thermal Expansion, Phase Diagram, and High-Temperature Rocksalt to Wurtzite Phase Transition. *Phys. Rev. B:Condens. Matter Mater. Phys.* **2014**, *89* (6), 064109.

(17) Fichtner, S.; Schönweger, G.; Dietz, F.; Hanssen, H.; Züge, H.; Kreutzer, T. N.; Lofink, F.; Kohlstedt, H.; Kapels, H.; Mensing, M. Wurtzite-Type Ferroelectrics for Microelectronic Devices: Scalability and Integration to Silicon Based Ferroelectric FETs. *2023 7th IEEE Electron Devices Technology & Manufacturing Conference (EDTM)*; Institute of Electrical and Electronics Engineers Inc.: Seoul, 2023, pp 1−3.

(18) Mikolajick, T.; Slesazeck, S.; Mulaosmanovic, H.; Park, M. H.; Fichtner, S.; Lomenzo, P. D.; Hoffmann, M.; Schroeder, U. Next Generation Ferroelectric Materials for Semiconductor Process Integration and Their Applications. *J. Appl. Phys.* **2021**, *129* (10), 100901.

(19) Kim, K. H.; Karpov, I.; Olsson, R. H.; Jariwala, D. Wurtzite and Fluorite Ferroelectric Materials for Electronic Memory. *Nat. Nanotechnol.* **2023**, *18* (5), 422−441.

(20) Pradhan, D. K.; Moore, D. C.; Kim, G.; He, Y.; Musavigharavi, P.; Kim, K. H.; Sharma, N.; Han, Z.; Du, X.; Puli, V. S.; Stach, E. A.; Joshua Kennedy, W.; Glavin, N. R.; Olsson, R. H.; Jariwala, D. A

Scalable Ferroelectric Non-Volatile Memory Operating at 600°C. *Nat. Electron.* **2024**, *7*, 348−355.

(21) Gerardin, S.; Paccagnella, A. Present and Future Non-Volatile Memories for Space. *IEEE Trans. Nucl. Sci.* **2010**, *57* (6), 3016−3039.

(22) Uchino, K.; Zheng, J. H.; Chen, Y. H.; Du, X. H.; Ryu, J.; Gao, Y.; Ural, S.; Priya, S.; Hirose, S. Loss Mechanisms and High Power Piezoelectrics. *J. Mater. Sci.* **2006**, *41* (1), 217−228.

(23) Lundh, J. S.; Zhu, W.; Song, Y.; Ko, S. W.; Fragkiadakis, C.; Mardilovich, P.; Trolier-Mckinstry, S.; Choi, S. Local Measurements of Domain Wall-Induced Self-Heating in Released PbZr$_{0.52}$Ti$_{0.48}$O$_3$films. *J. Appl. Phys.* **2020**, *128* (21), 214102.

(24) Fragkiadakis, C.; Sivaramakrishnan, S.; Schmitz-Kempen, T.; Mardilovich, P.; Trolier-McKinstry, S. Heat Generation in PZT MEMS Actuator Arrays. *Appl. Phys. Lett.* **2022**, *121* (16), 162906.

(25) Pernice, W. H. P.; Xiong, C.; Schuck, C.; Tang, H. X. High-Q Aluminum Nitride Photonic Crystal Nanobeam Cavities. *Appl. Phys. Lett.* **2012**, *100* (9), 091105.

(26) Fan, L.; Sun, X.; Xiong, C.; Schuck, C.; Tang, H. X. Aluminum Nitride Piezo-Acousto-Photonic Crystal Nanocavity with High Quality Factors. *Appl. Phys. Lett.* **2013**, *102* (15), 153507.

(27) Liu, X.; Bruch, A. W.; Gong, Z.; Lu, J.; Surya, J. B.; Zhang, L.; Wang, J.; Yan, J.; Tang, H. X. Ultra-High-Q UV Microring Resonators Based on a Single-Crystalline AlN Platform. *Optica* **2018**, *5* (10), 1279.

(28) Qamar, A.; Sherrit, S.; Zheng, X. Q.; Lee, J.; Feng, P. X. L.; Rais-Zadeh, M. Study of Energy Loss Mechanisms in AlN-Based Piezoelectric Length Extensional-Mode Resonators. *J. Microelectromech. Syst.* **2019**, *28* (4), 619−627.

(29) Zhu, W.; He, F.; Hayden, J.; Fan, Z.; Yang, J. I.; Maria, J. P.; Trolier-McKinstry, S. Wake-Up in Al$_{1-x}$B$_x$N Ferroelectrics Film. *Adv. Electron. Mater.* **2022**, *8* (6), 2100931.

(30) Zheng, J.; Takahashi, S.; Yoshikawa, S.; Uchino, K.; De Vries, J. W. C. Heat Generation in Multilayer Piezoelectric Actuators. *J. Am. Ceram. Soc.* **1996**, *79* (12), 3193−3198.

(31) Rodriguez, J. A.; Remack, K.; Boku, K.; Udayakumar, K. R.; Aggarwal, S.; Summerfelt, S. R.; Celii, F. G.; Martin, S.; Hall, L.; Taylor, K.; Moise, T.; McAdams, H.; McPherson, J.; Bailey, R.; Fox, G.; Depner, M. Reliability Properties of Low-Voltage Ferroelectric Capacitors and Memory Arrays. *IEEE Trans. Device Mater. Reliab.* **2004**, *4* (3), 436−447.

(32) Deng, B.; Zhang, Y.; Shi, Y. Examining the Ferroelectric Characteristics of Aluminum Nitride-Based Thin Films. *J. Am. Ceram. Soc.* **2024**, *107* (3), 1571−1581.

(33) Hayden, J.; Hossain, M. D.; Xiong, Y.; Ferri, K.; Zhu, W.; Imperatore, M. V.; Giebink, N.; Trolier-McKinstry, S.; Dabo, I.; Maria, J. P. Ferroelectricity in Boron-Substituted Aluminum Nitride Thin Films. *Phys. Rev. Mater.* **2021**, *5* (4), 044412.

(34) Song, Y.; Perez, C.; Esteves, G.; Lundh, J. S.; Saltonstall, C. B.; Beechem, T. E.; Yang, J. I.; Ferri, K.; Brown, J. E.; Tang, Z.; Maria, J. P.; Snyder, D. W.; Olsson, R. H.; Griffin, B. A.; Trolier-Mckinstry, S. E.; Foley, B. M.; Choi, S. Thermal Conductivity of Aluminum Scandium Nitride for 5G Mobile Applications and Beyond. *ACS Appl. Mater. Interfaces* **2021**, *13* (16), 19031−19041.

(35) Callaway, J. Model for Lattice Thermal Conductivity at Low Temperatures. *Phys. Rev.* **1959**, *113* (4), 1046−1051.

(36) Slack, G. A.; Tanzilli, R. A.; Pohl, R. O.; Vandersande, J. W. The Intrinsic Thermal Conductivity of AlN. *J. Phys. Chem. Solids* **1987**, *48* (7), 641−647.

(37) Morelli, D. T.; Heremans, J. P.; Slack, G. A. Estimation of the Isotope Effect on the Lattice Thermal Conductivity of Group IV and Group III-V Semiconductors. *Phys. Rev. B: Condens. Matter Mater. Phys.* **2002**, *66* (19), 1953041−1953049.

(38) Tran, D. Q.; Carrascon, R. D.; Iwaya, M.; Monemar, B.; Darakchieva, V.; Paskov, P. P. Thermal Conductivity of Al$_x$Ga$_{1-x}$N ($0 \leq x \leq 1$) Epitaxial Layers. *Phys. Rev. Mater.* **2022**, *6* (10), 104602.

(39) Okuno, J.; Kunihiro, T.; Konishi, K.; Materano, M.; Ali, T.; Kuehnel, K.; Seidel, K.; Mikolajick, T.; Schroeder, U.; Tsukamoto, M.; Umebayashi, T. 1T1C FeRAM Memory Array Based on

Ferroelectric HZO with Capacitor under Bitline. *IEEE J. Electron Devices Soc.* **2022**, *10*, 29−34.

(40) Francois, T.; Grenouillet, L.; Coignus, J. Demonstration of BEOL-Compatible Ferroelectric Hf0.5Zr0.5O2 FeRAM Co-Integrated with 130nm CMOS for Embedded NVM Applications. *2019 IEEE International Electron Devices Meeting (IEDM)*; IEEE, 2019, pp 362−365.

(41) Li, J.; Nagaraj, B.; Liang, H.; Cao, W.; Lee, C. H.; Ramesh, R. Ultrafast Polarization Switching in Thin-Film Ferroelectrics. *Appl. Phys. Lett.* **2004**, *84* (7), 1174−1176.

(42) Kim, K. D.; Lee, Y. B.; Lee, S. H.; Lee, I. S.; Ryoo, S. K.; Byun, S.; Lee, J. H.; Kim, H.; Park, H. W.; Hwang, C. S. Evolution of the Ferroelectric Properties of AlScN Film by Electrical Cycling with an Inhomogeneous Field Distribution. *Adv. Electron. Mater.* **2023**, *9* (5), 2201142.

(43) Ishibashi, Y.; Orihara, H. A Theory of D-E Hysteresis Loop. *Integr. Ferroelectr.* **1995**, *9*, 57−61.

(44) Chen, Z.; Zhang, Y.; Li, S.; Lu, X. M.; Cao, W. Frequency Dependence of the Coercive Field of $0.71Pb(Mg_{1/3}Nb_{2/3})O_3$-$0.29PbTiO_3$ Single Crystal from 0.01 Hz to 5 MHz. *Appl. Phys. Lett.* **2017**, *110* (20), 202904.

(45) Scott, J. F. Models for the Frequency Dependence of Coercive Field and the Size Dependence of Remanent Polarization in Ferroelectric Thin Films. *Integr. Ferroelectr.* **1996**, *12*, 71−81.

(46) Schön, D.; Menzel, S. Spatio-Temporal Correlations in Memristive Crossbar Arrays Due to Thermal Effects. *Adv. Funct. Mater.* **2023**, *33* (22), 2213943.

(47) Tran, Q.; Hayden, J.; Casamento, J.; Maria, J.-P.; Jackosn, T. N. Boron-Doped Aluminum Nitride Ferroelectric Field-Effect Transistors with ZnO Semiconductor Channel. *2024 device research conference (DRC)*; Nature Research, 2024; Vol. *18*.

(48) He, F.; Zhu, W.; Hayden, J.; Casamento, J.; Tran, Q.; Kang, K.; Song, Y.; Akkopru-Akgun, B.; Yang, J. I.; Tipsawat, P.; Brennecka, G.; Choi, S.; Jackson, T. N.; Maria, J. P.; Trolier-McKinstry, S. Frequency Dependence of Wake-up and Fatigue Characteristics in Ferroelectric $Al_{0.93}B_{0.07}N$ Thin Films. *Acta Mater.* **2024**, *266*, 119678.

(49) Choi, S.; Graham, S.; Chowdhury, S.; Heller, E. R.; Tadjer, M. J.; Moreno, G.; Narumanchi, S. A Perspective on the Electro-Thermal Co-Design of Ultra-Wide Bandgap Lateral Devices. *Appl. Phys. Lett.* **2021**, *119*, 170501.

(50) Cahill, D. G. Analysis of Heat Flow in Layered Structures for Time-Domain Thermoreflectance. *Rev. Sci. Instrum.* **2004**, *75* (12), 5119−5122.

(51) Wang, Y.; Park, J. Y.; Koh, Y. K.; Cahill, D. G. Thermoreflectance of Metal Transducers for Time-Domain Thermoreflectance. *J. Appl. Phys.* **2010**, *108* (4), 043507.

(52) Foteinopoulos, P.; Papacharalampopoulos, A.; Stavropoulos, P. On Thermal Modeling of Additive Manufacturing Processes. *CIRP J. Manuf. Sci. Technol.* **2018**, *20*, 66−83.

(53) Bai-Ru, Y.; Zhao-Yi, Z.; Hua-Zhong, G.; Xiang-Rong, C. Structural and Thermodynamic Properties of Wurtzitic Boron Nitride from First-Principle Calculations. *Commun. Theor. Phys.* **2007**, *48*, 925−929.

(54) Nipko, J. C.; Loong, C.-K. Phonon Excitations and Related Thermal Properties of Aluminum Nitride. *Phys. Rev. B:Condens. Matter Mater. Phys.* **1998**, *57*, 10550−10554.

(55) Dobrovinskaya, E. R.; Lytvynov, L. A.; Pishchik, V. Properties of Sapphire. *Sapphire*; Springer US, 2009; pp 55−176.

(56) Cook, J. G.; Moore, J. P.; Matsumura, T.; van der Meer, M. P. The Thermal and Electrical Conductivity of Aluminum. *Thermal conductivity 14*; Springer, 2013; p 65.

(57) Dallas, J.; Pavlidis, G.; Chatterjee, B.; Lundh, J. S.; Ji, M.; Kim, J.; Kao, T.; Detchprohm, T.; Dupuis, R. D.; Shen, S.; Graham, S.; Choi, S. Thermal Characterization of Gallium Nitride P-i-n Diodes. *Appl. Phys. Lett.* **2018**, *112* (7), 073503.

(58) Lundh, J. S.; Song, Y.; Chatterjee, B.; Baca, A. G.; Kaplar, R. J.; Armstrong, A. M.; Allerman, A. A.; Klein, B. A.; Kendig, D.; Kim, H.; Choi, S. Device-Level Multidimensional Thermal Dynamics with Implications for Current and Future Wide Bandgap Electronics. *J. Electron. Packag.* **2020**, *142* (3), 031113.

(59) Karch, K.; Bechstedt, F. Ab Initio Lattice Dynamics of BN and AlN: Covalent versus Ionic Forces. *Phys. Rev. B:Condens. Matter Mater. Phys.* **1997**, *56*, 7404−7415.

(60) Tütüncü, H. M.; Srivastava, G. P. Phonons in Zinc-Blende and Wurtzite Phases of GaN, AlN, and BN with the Adiabatic Bond-Charge Model. *Phys. Rev. B:Condens. Matter Mater. Phys.* **2000**, *62*, 5028−5035.

(61) Klemens, P. G. The Scattering of Low-Frequency Lattice Waves by Static Imperfections. *Proc. Phys. Soc., Sect. A* **1955**, *68*, 1113−1128.

(62) Cordero, B.; Gómez, V.; Platero-Prats, A. E.; Revés, M.; Echeverría, J.; Cremades, E.; Barragán, F.; Alvarez, S. Covalent Radii Revisited. *Dalton Trans.* **2008**, 2832−2838.

(63) Koh, Y. R.; Cheng, Z.; Mamun, A.; Bin Hoque, M. S.; Liu, Z.; Bai, T.; Hussain, K.; Liao, M. E.; Li, R.; Gaskins, J. T.; Giri, A.; Tomko, J.; Braun, J. L.; Gaevski, M.; Lee, E.; Yates, L.; Goorsky, M. S.; Luo, T.; Khan, A.; Graham, S.; Hopkins, P. E. Bulk-like Intrinsic Phonon Thermal Conductivity of Micrometer-Thick AlN Films. *ACS Appl. Mater. Interfaces* **2020**, *12* (26), 29443−29450.

(64) Inyushkin, A. V.; Taldenkov, A. N.; Chernodubov, D. A.; Mokhov, E. N.; Nagalyuk, S. S.; Ralchenko, V. G.; Khomich, A. A. On the Thermal Conductivity of Single Crystal AlN. *J. Appl. Phys.* **2020**, *127*, 205109.

(65) Song, Y.; Zhang, C.; Lundh, J. S.; Huang, H. L.; Zheng, Y.; Zhang, Y.; Park, M.; Mirabito, T.; Beaucejour, R.; Chae, C.; McIlwaine, N.; Esteves, G.; Beechem, T. E.; Moe, C.; Dargis, R.; Jones, J.; Leach, J. H.; Lavelle, R. M.; Snyder, D. W.; Maria, J. P.; Olsson, R. H.; Redwing, J. M.; Ansari, A.; Hwang, J.; Wang, X.; Foley, B. M.; Trolier-Mckinstry, S. E.; Choi, S. Growth-Microstructure-Thermal Property Relations in AlN Thin Films. *J. Appl. Phys.* **2022**, *132* (17), 175108.

(66) Chakraborty, P.; Xiong, G.; Cao, L.; Wang, Y. Lattice Thermal Transport in Superhard Hexagonal Diamond and Wurtzite Boron Nitride: A Comparative Study with Cubic Diamond and Cubic Boron Nitride. *Carbon* **2018**, *139*, 85−93.

(67) Raya-Moreno, M.; Rurali, R.; Cartoixà, X. Thermal Conductivity for III-V and II-VI Semiconductor Wurtzite and Zinc-Blende Polytypes: The Role of Anharmonicity and Phase Space. *Phys. Rev. Mater.* **2019**, *3*, 084607.

(68) Shoemaker, D. C.; Song, Y.; Kang, K.; Schuette, M. L.; Tweedie, J. S.; Sheppard, S. T.; McIlwaine, N. S.; Maria, J. P.; Choi, S. Implications of Interfacial Thermal Transport on the Self-Heating of GaN-on-SiC High Electron Mobility Transistors. *IEEE Trans. Electron Devices* **2023**, *70*, 5036−5043.

(69) Karim, A.; Song, Y.; Shoemaker, D. C.; Jeon, D. W.; Park, J. H.; Mun, J. K.; Lee, H. K.; Choi, S. Thermal Analysis of an α-Ga2O3MOSFET Using Micro-Raman Spectroscopy. *Appl. Phys. Lett.* **2023**, *123* (19), 192104.